This is a repository copy of *Information geometry in a reduced model of self-organised shear flows without the uniform coloured noise approximation*.

Information Geometry in a Reduced Model of Self-organised Shear Flows without the Uniform Coloured Noise Approximation

Eun-jin Kim[1], Quentin Jacquet[2,3], Rainer Hollerbach[2]

[1]*School of Mathematics and Statistics,*

University of Sheffield, Sheffield, S3 7RH, UK

[2]*Department of Applied Mathematics,*

University of Leeds, Leeds, LS2 9JT, UK

[3]*ENSTA ParisTech, Université Paris-Saclay,*

828 Boulevard des Maréchaux, 91120 Palaiseau, France

Abstract

We investigate information geometry in a toy model of self-organised shear flows, where a bi-modal PDF of x with two peaks signifying the formation of mean shear gradients is induced by a finite memory time γ^{-1} of a stochastic forcing f. We calculate time-dependent Probability Density Functions (PDFs) for different values of the correlation time γ^{-1} and amplitude D of the stochastic forcing, and identify the parameter space for unimodal and bimodal stationary PDFs. By comparing results with those obtained under the Uniform Coloured Noise Approximation (UCNA) in Jacquet, Kim & Hollerbach (Entropy **20**, 613, 2018), we find that UCNA tends to favor the formation of a bimodal PDF of x for given parameter values γ^{-1} and D. We map out attractor structure associated with unimodal and bimodal PDFs of x by measuring the total information length $\mathcal{L}_\infty = \mathcal{L}(t \to \infty)$ against the location x_0 of a narrow initial PDF of x. Here $\mathcal{L}(t)$ represents the total number of statistically different states that a system passes through in time. We examine the validity of the UCNA from the perspective of information change and show how to fine-tune an initial joint PDF of x and f to achieve a better agreement with UCNA results.

I. INTRODUCTION

Stochastic noise is ubiquitous and plays a crucial role in the evolution of many different systems (e.g. [1–4]). For example, in nonlinear systems, it can change the stability by making a stable equilibrium point unstable (or vice versa) or by inducing a stochastic resonance [5], while in a linear system, it can also increase the linear growth rate [6]. The effect of a stochastic noise on stability is analogous to the Reynolds stress in fluid mechanics, whereby the quadratic interaction of small-scale fluctuations affects the evolution of a large-scale mean field (e.g. [7]), leading to the formation of large-scale structures such as shear flows, vortices, jets, etc. The change in the stability of a nonlinear system can be inferred from a stationary Probability Density Function (PDF), such as the transition from a unimodal to bimodal PDF or vice versa. In this paper, we consider the case where a stationary PDF that is unimodal for δ-correlated stochastic noise becomes bimodal when the noise has a finite correlation time.

This issue was addressed in [8–10] and references therein. In particular, [9] proposed a 1-dimensional (1-D) continuous model of a self-organised shear flow [9] with a cubic nonlinear diffusion by extending a prototypical sand-pile model which evolves in discrete time.

Specifically, [9] considered the formation of a shear flow driven by a short-correlated (white-noise) random forcing, where shear gradient increases until it becomes unstable according to the stability criterion such as the Richardson criterion $R = (A/N)^2 > R_c = (A_c/N)^2 = 1/4$ in a strongly stratified medium. Here, N is the buoyancy frequency due to the restoring force (buoyancy), and A is the shear gradient with the critical value A_c. Fluctuations on small scales (or internal gravity waves) amplify a shear gradient and thus act as a forcing until the gradient exceeds its critical value A_c. When unstable, the shear flow then relaxes its gradient and generates small-scale fluctuations, and this relaxation was modelled by a nonlinear (cubic) diffusion; the shear gradient then grows again when small-scale turbulence becomes sufficiently strong to drive a shear flow. The same cycle repeats itself, exhibiting a continuous growth and damping. This highlights that a self-organised state is never stationary in time, but involves persistent fluctuations. For a short-correlated (white-noise) stochastic forcing, a stationary PDF was shown to be unimodal, signifying a zero value of a mean shear gradient.

[10] extended [9] to include a finite-correlation time τ of the stochastic noise, and solved a

2

stochastic differential equation by 4th-order stochastic Runga-Kutta method in 1D, showing the transition from a unimodal stationary PDF to a bimodal stationary PDF when the correlation time of a random forcing exceeds a critical value. A mean shear gradient is zero for a unimodal PDF, while its non-zero value represents the critical shear gradient around which a shear gradient continuously grows and decays through the interaction with fluctuations. The transition from a unimodal to bimodal PDF represents the formation of a non-zero mean shear gradient, or the formation of jets. Similar results were also reproduced in a simpler 0-D model with a cubic damping and also in a 2-D fluid simulation. In particular, 2D results showed that a shear flow evolves through the competition between its growth and damping due to a localized instability, maintaining a stationary PDF, and that the bimodal PDF results from a self-organising shear flow with linear profile.

In this paper, we extend [9, 10] to investigate the time-evolution of PDFs to elucidate the effects of different initial conditions and correlation times. A particular interest will be to understand the information change in the relaxation of an initial PDF to a stationary PDF by using the *information length* $\mathcal{L}$ [11–21]. In the case of a stochastic variable x and time-dependent PDF $p(x,t)$, $\mathcal{L}$ is defined by

$$\mathcal{L}(t) = \int_0^t \frac{dt_1}{\tau(t_1)} = \int_0^t \sqrt{\int dx \frac{1}{p(x,t_1)} \left[\frac{\partial p(x,t_1)}{\partial t_1} \right]^2} \, dt_1. \tag{1}$$

$\mathcal{L}(t)$ measures the cumulative change in $p(x,t)$, or the total number of statistically distinguishable states between $p(x,0)$ and $p(x,t)$, and thus provides a convenient means of measuring the distance between $p(x,0)$ and $p(x,t)$ continuously in time for a given initial condition $p(x,0)$. In contrast to other statistical measures such as entropy, which depends only on the PDF at a single instant in time, $\mathcal{L}(t)$ depends on all the intermediate states that a system evolves through between time 0 and t, and is thus a Lagrangian quantity.

[11–22] utilized this property to map out the attractor structure by considering a narrow initial PDF at a different peak position x_0 and by measuring $\mathcal{L}_\infty$ against x_0. In particular, $\mathcal{L}_\infty$ captured the effect of different deterministic forces through the scaling of $\mathcal{L}_\infty$ with the position of a narrow initial PDF. For a stable equilibrium, the minimum value of $\mathcal{L}_\infty$ occurs at the equilibrium point. For a chaotic attractor, $\mathcal{L}_\infty$ – the distance between x_0 and the final chaotic attractor – was shown to depend sensitively on x_0, since a small change in the initial condition x_0 causes a large difference in a path that a system evolves through and thus $\mathcal{L}_\infty$. This is a good illustration of a chaotic equilibrium and is quite similar to the sensitive

dependence of the Lyapunov exponent on the initial condition. That is, our $\mathcal{L}_\infty$ provides a new methodology to test chaos and a diagnostic for understanding dynamical systems.

In this paper, to facilitate our analysis and numerical simulations, we utilise a 0-D model with a cubic damping, and calculate time-dependent PDFs which depend on two variables x and f. For two variables, Eq. (1) generalises to

$$\mathcal{L}(t) = \int_0^t \frac{dt_1}{\tau(t_1)} = \int_0^t \sqrt{\iint dx df \frac{1}{p(x,f,t_1)} \left[\frac{\partial p(x,f,t_1)}{\partial t_1}\right]^2} \, dt_1. \tag{2}$$

We can then calculate $\mathcal{L}(t)$ either from Eq. (2), or from Eq. (1) by using a marginal PDF $P(x,t) = \int p(x,f,t)\, df$. We will compare the two versions of $\mathcal{L}_\infty$ with one another, as well as with $\mathcal{L}_\infty$ from a 1-Variable (1-V) approximation to the full 2-Variable (2-V) model (see Section 2). The remainder of this paper is organised as follows. We introduce our model in Section II and provide some analytical results. In Section III we discuss 1-V and 2-V models. Sections IV and V present the analysis for stationary and time-dependent PDFs, respectively. Conclusion is provided in Section VI.

II. SIMPLE (LINEAR) ANALYSIS

As noted in the introduction, given the universality of self-organisation in 0-D, 1-D and 2-D models, and the challenge in computation of time-dependent PDFs, we utilise a 0-D model to facilitate the calculation of time-dependent PDFs and scan over different parameter values. Our 0-D model is based on the cubic process for a stochastic variable x (e.g. representing a shear gradient), governed by the following Langevin equations

$$\partial_t x = -(ax + bx^3) + f \equiv -g(x) + f, \tag{3}$$

$$\partial_t f = -\gamma f + \xi. \tag{4}$$

Here, $g(x) = ax + bx^3$, where a and b are constants. We are interested in the case where both are positive, in which case both of them can be rescaled to one without loss of generality. ξ is a δ-correlated stochastic noise ($\langle \xi \rangle = 0$) with the correlation function

$$\langle \xi(t)\xi(t') \rangle = 2D\delta(t - t'), \tag{5}$$

where the angular brackets represent the average over ξ.

4

If f were δ-correlated, Eq. (3) would have only one equilibrium point $x = 0$ (when $f = 0$), leading to a unimodal stationary PDF $p(x, t \to \infty) = p_\infty(x)$ with a peak at $x = 0$. A bimodal stationary PDF can only form due to a finite correlation time of f. Our model given by Eqs. (3)-(4) is thus fundamentally different from a bistable model considered in [8] where a bimodal PDF can form due to bistability.

A. Statistical property of f

It is worth noting that f in Eq. (4) evolves independently of x, and is simply the Ornstein-Uhlenbeck process [2], with solution

$$f(t) = f(0)e^{-\gamma t} + \int_0^t dt_1 e^{-\gamma(t-t_1)} \xi(t_1), \tag{6}$$

where $f(0) = f(t = 0)$. Since f is a Gaussian process, a time-dependent marginal PDF of f, $\tilde{p}(f, t) = \int p(x, f, t)\, dx$, is readily obtained from Eq. (6) as

$$\tilde{p}(f, t) = \sqrt{\frac{\alpha}{\pi}} e^{-\alpha(f - \langle f \rangle)^2}, \tag{7}$$

where

$$\langle f(t) \rangle = \langle f(0) \rangle e^{-\gamma t}, \tag{8}$$

$$\frac{1}{2\alpha(t)} = \frac{e^{-2\gamma t}}{2\alpha(0)} + \frac{D(1 - e^{-2\gamma t})}{\gamma}. \tag{9}$$

Here, $\alpha_0 = \alpha(t = 0)$; α is the inverse temperature of f related to its variance as $\langle (\delta f(t))^2 \rangle = \frac{1}{2\alpha(t)}$, where $\delta f(t) = f(t) - \langle f(t) \rangle$. In the limit of $t \to \infty$, $\alpha \to \frac{\gamma}{2D}$ and $\langle f \rangle \to 0$, Eq. (7) giving the stationary PDF

$$\tilde{p}(f) \propto \exp[-\gamma f^2 / 2D]. \tag{10}$$

Also, from Eqs. (5) and (6), we can show

$$\langle \delta f(t) \delta f(t') \rangle \sim \int_0^t dt_1 \int_0^{t'} dt_2 e^{-\gamma(t-t_1)} e^{-\gamma(t'-t_2)} \langle \xi(t_1)\xi(t_2) \rangle$$

$$= \frac{D}{\gamma} \left[e^{-\gamma(t'-t)} - e^{-\gamma(t+t')} \right] \approx \frac{D}{\gamma} e^{-\gamma|t'-t|}, \tag{11}$$

where we assumed $t' > t$ and ignored the contribution from the terms involving $e^{-\gamma(t'+t)}$. Thus, f in Eq. (4) has the correlation time $\tau \sim \gamma^{-1}$, whose finite value is crucial for the formation of a bimodal PDF in x. A δ-correlated f is obtained in the limit $\gamma \to \infty$. We can

also show that f and x are correlated for $t > 0$ even when they are uncorrelated initially at $t = 0$. To this end, we let $x(t) = \langle x \rangle + \delta x$ and $f(t) = \langle f \rangle + \delta f$ in Eqs. (3) and (6), and subtract the mean values to obtain

$$\partial_t \delta x \;=\; -\frac{dg(x)}{dx}\bigg|_{x=\langle x \rangle} \delta x + \delta f, \tag{12}$$

$$\delta f(t) \;=\; \delta f(0)e^{-\gamma t} + \int_0^t dt_1 e^{-\gamma(t-t_1)}\xi(t_1), \tag{13}$$

where $g(x) = ax + bx^3$ ($a = b = 1$). For a sufficiently small time, we approximate $\frac{dg(x)}{dx}\big|_{x=\langle x \rangle} \sim \frac{dg(x)}{dx}\big|_{x_0} \equiv \Gamma$ where $x_0 = \langle x(t=0) \rangle$ and obtain a solution to Eq. (12) as

$$\begin{aligned}
\delta x(t) \;&=\; \delta x(0)e^{-\Gamma t} + \int_0^t dt_1 e^{-\Gamma(t-t_1)}\delta f(t_1) \\
&=\; \delta x(0)e^{-\Gamma t} + \frac{\delta f(0)}{\Gamma - \gamma}\left[e^{-\gamma t} - e^{-\Gamma t} \right] + \int_0^t dt_2\, \xi(t_2)\left[e^{-\gamma(t-t_2)} - e^{-\Gamma(t-t_2)} \right].
\end{aligned} \tag{14}$$

Performing some algebra from Eqs. (13)-(14) and (5) and using $\langle \delta f(0)\delta x(0) \rangle = 0$, we find

$$\langle \delta f(t)\delta x(t) \rangle = \frac{\langle (\delta f(0))^2 \rangle}{\Gamma - \gamma}\left[e^{-2\gamma t} - e^{-(\Gamma+\gamma)t} \right] + \frac{2D}{\Gamma - \gamma}\left[\frac{1}{2\gamma}\left(1 - e^{-2\gamma t} \right) - \frac{1 - e^{-(\gamma+\Gamma)t}}{\Gamma + \gamma} \right]. \tag{15}$$

Eq. (15) is non-zero for $t > 0$ unless $\Gamma = \gamma$, showing that δf and δx are correlated.

III.   1-VARIABLE (1-V) AND 2-VARIABLE (2-V) MODELS

The set of Eqs. (3)-(4) give a joint PDF $p(x, f, t)$ for the two variables (x, f), which satisfies the following Fokker-Planck equation [2]

$$\frac{\partial}{\partial t}p(x, f, t) = \frac{\partial}{\partial x}\left[(g(x) - f)p(x, f, t) \right] + \frac{\partial}{\partial f}\left[\gamma f p(x, f, t) \right] + D\frac{\partial^2}{\partial f^2}p(x, f, t). \tag{16}$$

Just as with the bistable model in [8], Eq. (16), or equivalently Eqs. (3)-(4), does not satisfy detailed balance, so it is impossible to find an analytical stationary solution in a closed form. To gain a key insight, our previous work [22] utilised the Uniform Coloured Noise Approximation (UCNA) [23], and performed thorough parameter studies of time-dependent PDFs of one variable x, and $\mathcal{L}(t)$ calculated from Eq. (1). As noted in [23], UCNA works well in the limit where the correlation time γ^{-1} is either small or large in general. Specifically, for our $g(x) = ax + bx^3$ in Eq. (3), the validity of UCNA is given by the effective damping factor Γ [see Eq. (3) in [23]]

$$\Gamma = \gamma^{\frac{1}{2}} + \gamma^{-\frac{1}{2}}\partial_x g(x) \to \infty. \tag{17}$$

6

Using $\partial_x g(x) = a + 3bx^2 > 0$ (recall a, b are positive constants) in Eq. (17), we can see that UCNA is a good approximation as $\gamma \to 0$, $\gamma \to \infty$, or $x \to \infty$. This will be observed later in Figure 1. As it is of interest to compare the results from our 2-Variable model with the approximated 1-Variable model in [22], we summarise the main equations for the 1-V model with UCNA in the following subsection.

A. 1-Variable (1-V) Model with UCNA

In order to compare our results in this paper with those in [22], it is useful to use a different variable, say y, instead of x for the 1-V model in [22]. Thus, by replacing x by y in Eq. (3), UCNA reduces Eqs. (3)-(4) to

$$\partial_t y = -\frac{\gamma g}{G} + \frac{1}{G}\xi, \tag{18}$$

where $G = \partial_y g(y) + \gamma$ and $g(y) = ay + by^3$. The corresponding Fokker-Planck equation is given by

$$\frac{\partial}{\partial t}p(y,t) = \frac{\partial}{\partial y}\left[\frac{\gamma g}{G}p(y,t)\right] + D\frac{\partial}{\partial y}\left[\frac{1}{G}\frac{\partial}{\partial y}\left(\frac{1}{G}p(y,t)\right)\right]. \tag{19}$$

Note that we use the Stratonovich calculus [2–4, 24], which recovers the limit of a δ-correlated forcing from a finite-time correlated forcing [24].

Eq. (19) permitted us to find an exact stationary PDF and to perform a thorough study on time-dependent PDFs and $\mathcal{L}$ by using a relatively narrow initial PDF $p(y,0) \propto \exp[-(y-y_0)^2/10^{-3}]$ with the initial mean value y_0. In particular, we investigated the information change in these processes and measured $\mathcal{L}_\infty$ for different y_0 to map out the attractor structure. In the context of a shear flow, y_0 represents the mean value of an initial shear gradient. For a unimodal stationary PDF, the mean shear gradient decreases to zero in the long time limit; for a bimodal stationary PDF with a peak $\pm y_*$, the case of $y_0 > y_*$ models the relaxation of an initial super-critical gradient y_0 to the critical value y_*, and the case of $y_0 < y_*$ models the build-up of the gradient from a subcritical initial value to the critical value y_*. This led us to identify the difference between the relaxation and build-up of shear gradient in view of information change.

B. 2-Variable (2-V) Model and Main Goal

Returning to the Fokker-Planck equation (16), there are several aspects we wish to consider. First, what do the stationary solutions look like, for which parameter values γ and D are they unimodal versus bimodal, and how do these results compare with the 1-V UCNA model [22]?

Next, to study the equivalent of the $\mathcal{L}_\infty$ versus y_0 results referred to above, we must choose an initial condition $p(x, f, 0)$. The obvious choice for the x-dependence is $\exp[-(x - x_0)^2/10^{-3}]$, analogous to the initial condition in [22]. The 'correct', i.e. most interesting, choice for the f-dependence is less obvious, and we will in fact consider two different choices below, motivated in part by the structure of the stationary solutions.

Another interesting aspect of the 2-V model are the two different versions of $\mathcal{L}(t)$, either the full Eq. (2) or the reduced Eq. (1). Since Eq. (1) treats f as an effectively hidden, unobservable variable, comparing the results between (1) and (2) could elucidate some of the consequences of using incomplete data (i.e. only x) due to the inability of measuring certain variables. Of particular interest is then the attractor structure inferred from either or both versions of $\mathcal{L}_\infty$ as a function of the initial position x_0, again for two different choices for the initial f-dependence.

The numerical solution of Eq. (16) is implemented by finite-differencing in x and f, and second-order Runge-Kutta timestepping, modified to treat the diffusive term $D\frac{\partial^2}{\partial f^2}p$ implicitly. Because diffusion acts only in the f variable, it is possible to treat this term implicitly while still preserving a tridiagonal structure to the timestepping equations. Grids as fine as $\Delta x = 6 \cdot 10^{-3}$ and $\Delta f = 8 \cdot 10^{-3}$ were used, and timesteps as small as $\Delta t = 4 \cdot 10^{-5}$. These quantities were all varied to ensure properly resolved solutions.

Care must also be taken to ensure that the computational domain $x \in [-x_{max}, x_{max}]$, $f \in [-f_{max}, f_{max}]$, with $p = 0$ enforced on the boundaries, is sufficiently large to be a good approximation to an infinite range for both x and f. Taking $x_{max} = 3$ was sufficient for the values of $x_0 \in [0, 1.8]$ that we will consider. For f_{max} values up to 14 were required, for reasons that will become clear once we see the structure of the stationary solutions.

A useful test to check whether x_{max} and f_{max} were taken to be sufficiently large is simply to see how well the total probability $\iint p \, dx df$ remains constant ($=1$). If a solution is properly resolved, and the computational domain is sufficiently large, the total probability

is correctly conserved to within 10^{-5} or better.

Another useful check on both the resolutions and the box size comes from integrating Eq. (16) in x. Recalling $\tilde{p}(f,t) = \int p(x,f,t)\,dx$, the integral of (16) yields

$$\frac{\partial}{\partial t}\tilde{p} = \frac{\partial}{\partial f}(\gamma f \tilde{p}) + D\frac{\partial^2 \tilde{p}}{\partial f^2}. \tag{20}$$

And unlike the 2-dimensional (16), this has the exact analytic solution (7), being just a 1-dimensional Ornstein-Uhlenbeck process. It is then straightforward to convert a numerically computed $p(x,f,t)$ to its corresponding $\tilde{p}(f,t)$, and verify that it agrees with the analytic expression, with agreement to within 10^{-5} for all cases.

Finally, note that the stationary solution of Eq. (20) is readily shown to be Eq. (10). In particular, we note that this is *always* unimodal in f, for all γ and D. The stationary solutions can only be bimodal if we consider either the full $p(x,f)$, or else the previously introduced $P(x) = \int p(x,f)\,df$, as we will see in the following section.

IV. STATIONARY SOLUTIONS

Figure 1 shows the numerically computed stationary solutions for three combinations of γ and D. For any given γ and D the final state is unique, and does not depend on the chosen initial condition (provided only that it is properly normalised to have total probability equal to one). The top row shows contours of the full 2-dimensional $p(x,f)$; the bottom row shows the integrated $P(x)$. The bottom row also shows the equivalent 1-V UCNA solution [22] for comparison.

For $\gamma = 1$, $D = 0.2$, the solution is strongly unimodal, as seen in either $p(x,f)$ or $P(x)$. For $\gamma = 0.6$, $D = 0.6$, $p(x,f)$ is very slightly bimodal, and $P(x)$ has also just developed two peaks. In contrast the equivalent $P(x)$ in the UCNA model is already more strongly bimodal. Finally, for $\gamma = 0.2$, $D = 1$, both $p(x,f)$ and $P(x)$ are strongly bimodal. Therefore, for the same parameter values of D and γ, 2-V model shows a weaker tendency for a bimodal PDF compared with 1-V model. This is thought to be due to the fact that $\tilde{p}(f)$ is always unimodal, and the coupling between f and x through Eq. (15) tends to facilitate the formation of a unimodal PDF in 2-V model. It is interesting to see that the difference between 1-V and 2-V model becomes smaller as x increases, as noted in Section II. In Figure 2, we quantify the transition from unimodal to bimodal solutions as γ is decreased and/or D is increased,

9

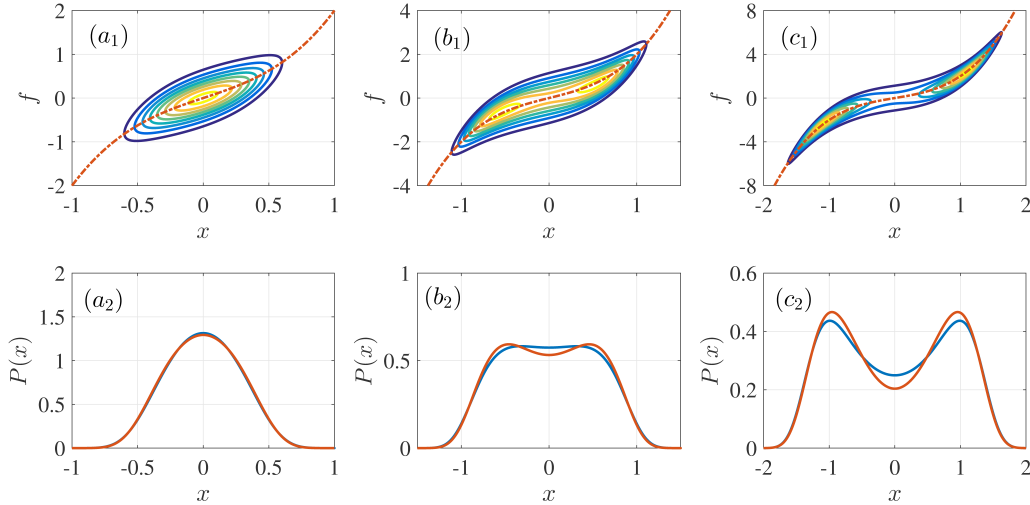by mapping out the boundary in the $\{\gamma, D\}$ plane where it occurs.

FIG. 1: The top row shows contours of $p(x, f)$; the bottom row shows $P(x)$ in blue, and the equivalent 1-V UCNA solution in red. The dotted red lines in the top row show the curves $f = g(x)$, around which the solutions must distribute themselves. Panels $(a_{1,2})$ are for $\gamma = 1$, $D = 0.2$, $(b_{1,2})$ are for $\gamma = 0.6$, $D = 0.6$, and $(c_{1,2})$ are for $\gamma = 0.2$, $D = 1$. The corresponding contour intervals in the top row are 0.2, 0.06, and 0.05, respectively. Finally, note how the box sizes increase in going from (a_1) to (c_1); the actual computational domains were even larger, to ensure that p was sufficiently small near the boundaries.

Another interesting feature to note in Figure 1 is how the solutions are aligned along the curve $f = g(x) = x + x^3$. To understand this, we can refer to the original Langevin equation (3), according to which $\partial_t x = 0$ implies $f = g(x)$. Alternatively, from the Fokker-Planck equation (16), the stationary solutions must satisfy

$$0 = \frac{\partial}{\partial x} [(g(x) - f)p] + \frac{\partial}{\partial f} [\gamma f p] + D \frac{\partial^2}{\partial f^2} p. \tag{21}$$

Integrating with respect to f, and using $p \to 0$ as $f \to \pm\infty$, this yields

$$\frac{d}{dx} \int (g(x) - f)p \, df = 0. \tag{22}$$

That is, this integral does not depend on x. For $x \to \pm\infty$ it must be 0 though, since $p \to 0$ (and far more rapidly than $g(x)$ diverges). The final result is therefore that the stationary solutions must satisfy

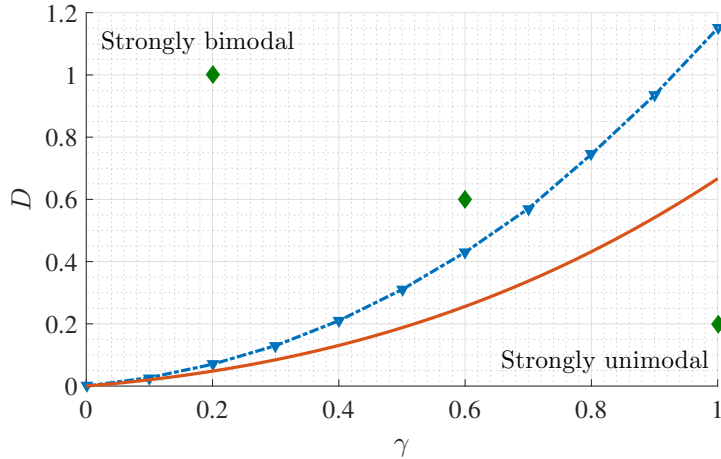$$\int (g(x) - f)p \, df = 0. \tag{23}$$

10

FIG. 2: The dashed blue line shows the numerically computed boundary between regions where $P(x)$ is unimodal versus bimodal. The solid red line shows the analytic equivalent in the 1-V UCNA model [22]. The green diamonds correspond to the three solutions shown in Figure 1.

Together with the fact that p is strictly positive, this means that p must be symmetrically distributed about the curve $f = g(x)$, so that regions where $f > g(x)$ can cancel regions where $f < g(x)$. Eq. (23) also provides another opportunity to test the numerics: all solutions did indeed evolve so that the maximum over x of $|\int(g(x) - f)p\,df|$ decreased in time, and were run sufficiently long for this quantity to be less than 10^{-4}.

V. TIME-DEPENDENT SOLUTIONS

As noted above, for time-dependent solutions a natural x-dependence of an initial condition is $\exp[-(x - x_0)^2/10^{-3}]$, but the f-dependence is less obvious. Based on the results (20) and (10), one reasonable possibility would be $\exp[-\gamma(f - f_0)^2/2D]$, with $f_0 = \langle f(0) \rangle$ still to be decided. According to (9) the width of this Gaussian would remain unchanged, and the peak would simply move toward its equilibrium position $f = 0$ as $f_0 e^{-\gamma t}$ (see Eq. (8)). That is, if we chose $f_0 = 0$, $\tilde{p}$ would not change at all, but would already be in its final form (10). On the other hand, according to the results of Figure 1, and also Eq. (23), if $x_0 \neq 0$, then perhaps f_0 should be non-zero as well, and indeed $f_0 = g(x_0)$ could be a

suitable choice. Another quite similar option is

$$f_0 = g(x_0) \left[1 - \frac{\gamma}{g'(x_0) + \gamma} \right], \tag{24}$$

where $g'(x_0) = \frac{dg}{dx}\big|_{x=x_0}$. From the original Langevin equations (3) and (18), this choice yields $\partial_t \langle x \rangle = \partial_t \langle y \rangle$ at $t = 0$, and thereby offers perhaps the most direct comparison between the 2-V model here and the previous 1-V model. We therefore chose our initial conditions to be

$$p(x, f, 0) \propto \exp \left[-\frac{(x - x_0)^2}{10^{-3}} - \frac{\gamma(f - f_0)^2}{2D} \right], \tag{25}$$

with f_0 either zero, or given by (24).

A. PDF evolution

Figures 3 and 4 show examples of how the solutions evolve when starting from the two choices of initial conditions $f_0 = 0$ and $f_0 \neq 0$, with $x_0 = 1.2$ in both cases. Since $\gamma = 0.5$ and $D = 0.5$ are the same for both figures, they evolve to the same final equilibrium, similar to those in Figure 1. Panels (a-e) show contour plots of $p(x, f, t)$ at times $t = 0, 0.15, 0.3, 1.5$ and 3, respectively, with contour intervals 0.5, 0.5, 0.3, 0.05 and 0.05. Panel (f) in Figures 3 and 4 shows in red the position of the average ($\langle x \rangle, \langle f \rangle$), and in blue the position of the peak, where the triangles correspond to the times in panels (a-e). For both $f_0 = 0$ and $f_0 \neq 0$, we observe that the average moves to $(0, 0)$, whereas the peak moves to $x = 0.57$, $f = 0.70$, that is, to the positive x, f peak of the final bimodal equilibrium $p(x, f)$. Interestingly, when $f_0 = 0$, the x coordinate of the peak in Figure 3(f) undergoes a non-monotonic evolution, initially decreasing until it overshoots the peak position $x_* = 0.57$ and then increasing to x_*. The overshooting of x_* seems to be a result of the coupling between x and f, which tries to push the x peak toward $x = 0$ for $f_0 = 0$. In comparison, the evolution of the x peak in Figure 4(f) is monotonic. A more convoluted evolution of the peak in Figure 3(f) suggests that an initial PDF with $f_0 = 0$ is more strongly out of equilibrium, with a larger distance to the final stationary PDF; this will be confirmed by calculating the total information length $\mathcal{L}_\infty$ in Section IV.B. Interestingly, the choice $f_0 = 0$ however reaches the final equilibrium much quicker. This is probably because it already starts out with $\tilde{p}$ in its final form (10), whereas the choice $f_0 \neq 0$ must adjust not only in x but also in f, which necessarily involves the γ^{-1} correlation time scale of f.
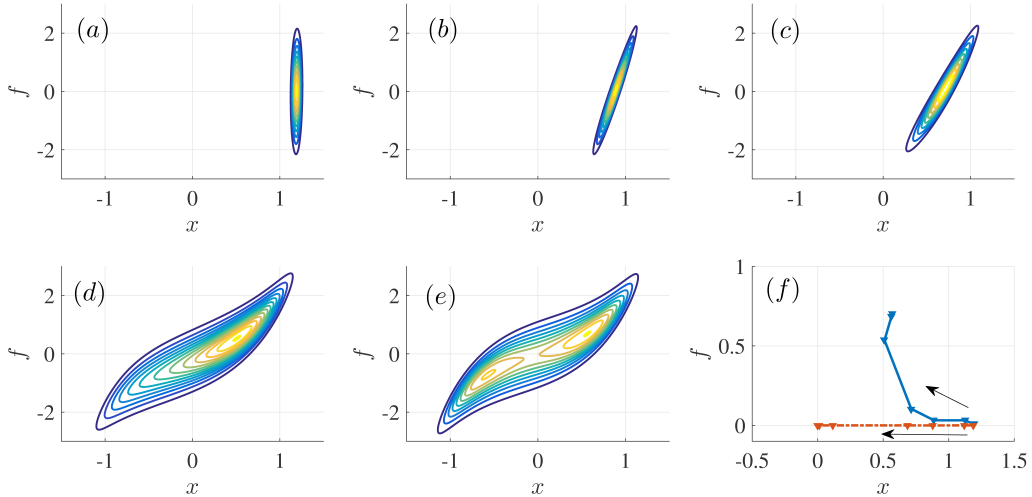
FIG. 3: The time-evolution of the solution with $\gamma = 0.5$, $D = 0.5$, $x_0 = 1.2$, and $f_0 = 0$. Panels (a-e) show contour plots of $p(x, f, t)$ at times $t = 0$, 0.15, 0.3, 1.5 and 3, respectively, with contour intervals 0.5, 0.5, 0.3, 0.05 and 0.05. Panel (f) shows in red the position of the average $(\langle x \rangle, \langle f \rangle)$, and in blue the position of the peak. Note how the average moves to $(0, 0)$, whereas the peak moves to one of the peaks of the final bimodal equilibrium. The triangles correspond to the times in panels (a-e).

Figure 5 shows the f-integrated $P(x)$ profiles corresponding to Figures 3 and 4. Both start with the narrow peak at $x_0 = 1.2$ and evolve toward the final profile that is just barely in the bimodal regime, as it should be according to the regime diagram in Figure 2. Comparing the $f_0 = 0$ profiles on the left with the $f_0 \neq 0$ profiles on the right, we notice also how the initial peak moves inward much more rapidly for $f_0 = 0$ than for $f_0 \neq 0$. According to the Langevin equation (3), the initial movement of the peak will satisfy $\partial_t \langle x \rangle = -g(x_0) + f_0$, so any positive f_0 will slow down the initial inward movement. Recall also that the particular choice of f_0 given by (24) was chosen precisely so that the initial inward speed matches that of the 1-V UCNA model.

B. Attractor structure

We now investigate attractor structure associated with unimodal and bimodal PDFs by mapping out how the total information length $\mathcal{L}_\infty$ depends on the initial position x_0, and how the two different forms of $\mathcal{L}$ compare with one another, and with the previous 1-V
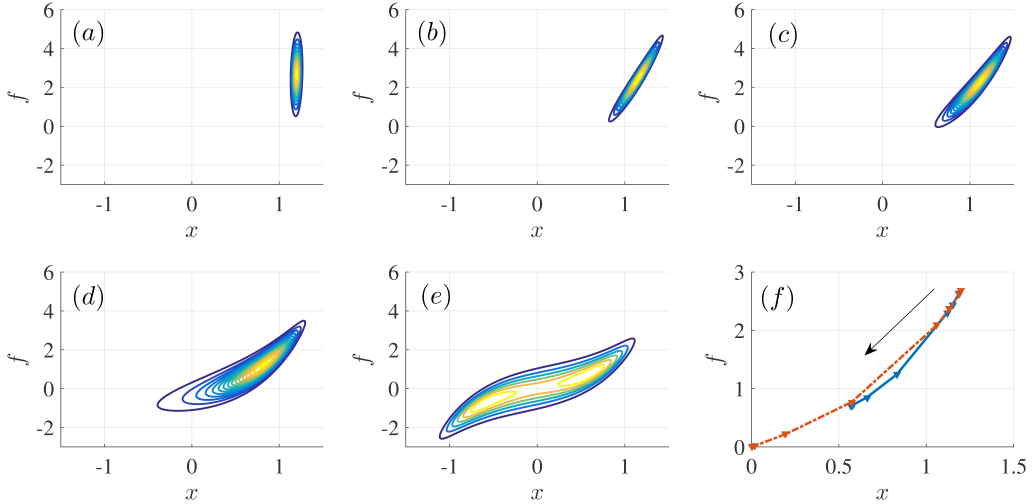
FIG. 4: The time-evolution of the solution with $\gamma = 0.5$, $D = 0.5$, $x_0 = 1.2$, and f_0 given by (25). Panels (a-e) show contour plots of $p(x, f, t)$ at times $t = 0$, 0.5, 1, 5 and 10, respectively, with contour intervals 0.5, 0.4, 0.2, 0.08 and 0.07. Panel (f) shows in red the position of the average $(\langle x \rangle, \langle f \rangle)$, and in blue the position of the peak. Note how the average moves to $(0, 0)$, whereas the peak moves to one of the peaks of the final bimodal equilibrium. The triangles correspond to the times in panels (a-e).
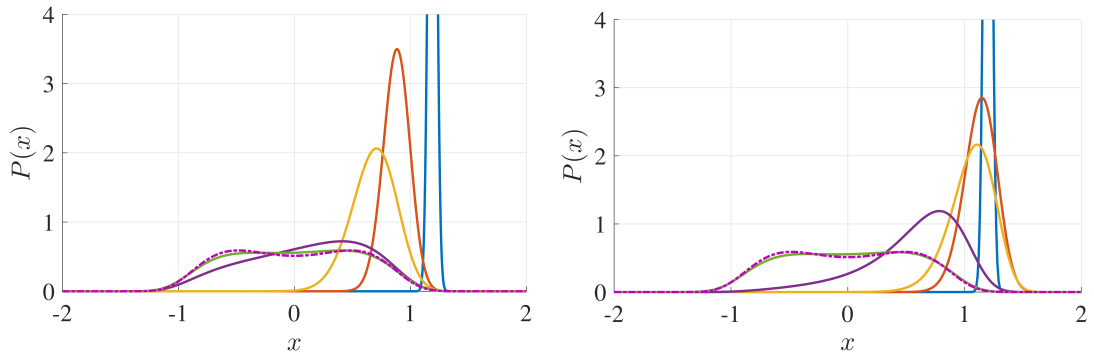

FIG. 5: The left/right panels show $P(x)$ for the solutions in Figures 3 and 4, respectively. The initial condition is the narrow peak at $x = 1.2$, which relaxes to the final equilibrium profile shown as the dashed curve. The intermediate profiles are at times 0.15, 0.3, 1.5 and 3 on the left, and 0.5, 1, 5 and 10 on the right, corresponding to panels ($b - e$) in Figures 3 and 4, respectively.

UCNA results. Figure 6 shows these results, for $x_0 \in [0, 1.8]$, and the same three $\{\gamma, D\}$ combinations as in Figure 1.

14

The top row shows the Eq. (1) version of $\mathcal{L}$, with $P(x,t)$ as its input. That is, f is here treated as an unobservable variable. If we compare the two initial conditions $f_0 = 0$ in blue and $f_0 \neq 0$ in red, it is quite interesting that $f_0 = 0$ consistently has greater $\mathcal{L}_\infty$, even though this is the initial condition that already starts out with $\tilde{p}$ in its final form, whereas $f_0 \neq 0$ must adjust in f as well as in x. Recalling that $\mathcal{L}_\infty$ cares about intermediate states that a system passes through in reaching the final stationary PDF, this confirms that the initial PDF with $f = 0$ is more strongly out of equilibrium, as noted in Section IV.A. The fact that $f_0 = 0$ has greater $\mathcal{L}_\infty$ while it reaches the equilibrium quicker highlights that $\mathcal{L}_\infty$ is a fundamentally different physical quantify from the equilibration time. Furthermore, it is interesting to note how the dashed green lines, showing UCNA results, agree rather well with the $f_0 \neq 0$ results. Choosing f_0 such that the initial speeds of the peaks match up seems to make UCNA a better approximation, everywhere except the small x_0 cases in panel c_1 (the strongly bimodal case). A weaker tendency for a bimodal structure in $\mathcal{L}_\infty$ versus x_0, with the minimum $\mathcal{L}_\infty$ at $x_0 = 0$, in the 2-V model seems to be due to a unimodal PDF of f which affects the evolution of x through Eq. (3).

The bottom row in Figure 6 shows the Eq. (2) version of $\mathcal{L}$, with $p(x,f,t)$ as its input. Here therefore both x and f are treated as observable variables. We again find that $\mathcal{L}_\infty$ is greater for $f_0 = 0$ than for $f_0 \neq 0$. Comparing the two rows, we also see that the 'two-observables' version of $\mathcal{L}$ is significantly greater than the 'one-observable' version. This is an interesting reflection of the fact that being unable to observe variation of the PDF in a hidden variable decreases the information (and information change) and thus leads to a smaller information length. This illustrates once again the natural, intuitive interpretation of information length as a measure of change in PDFs.

VI.   CONCLUSION

We investigated time-evolution of PDFs in a toy model of self-organised shear flows by considering a cubic process driven by a finite-correlated noise f. The formation of shear flows with a non-zero mean gradient was induced by a finite memory time γ^{-1} of a stochastic forcing, signified by the emergence of a bimodal PDF of x with the two peaks representing a non-zero mean shear gradient. We focused on the relaxation problem of a self-organised shear flow where the time evolution of mean shear gradient $x_0 > x_*$ $(x_0 < x_*)$ models the
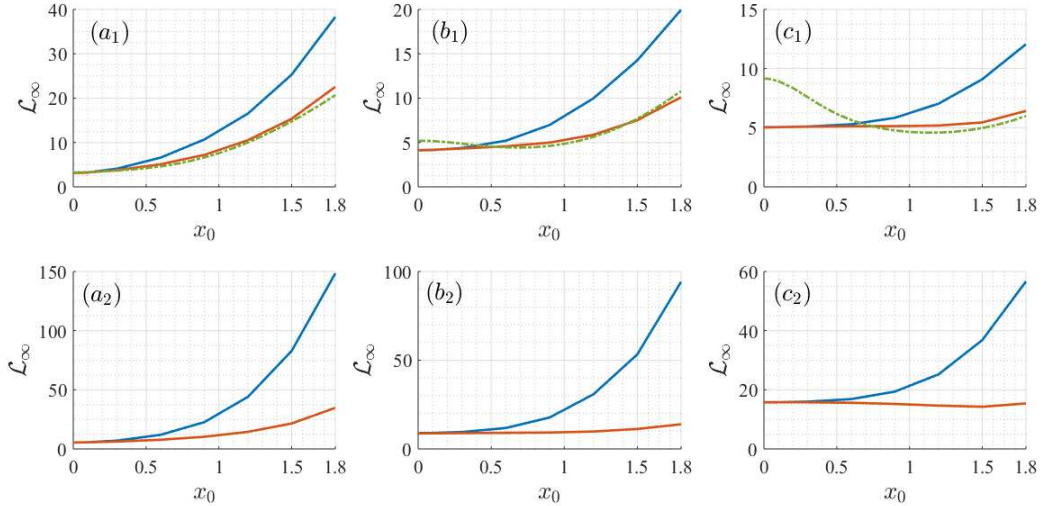
FIG. 6: The top row shows $\mathcal{L}_\infty$ as a function of x_0, computed according to the 'one-observable' form (1). Blue is $f_0 = 0$, red is f_0 given by (24), and dashed green is UCNA as in [22]. The bottom row shows $\mathcal{L}_\infty$ as a function of x_0, computed according to the 'two-observable' form (2). Panels $(a_{1,2})$ are for $\gamma = 1$, $D = 0.2$, $(b_{1,2})$ are for $\gamma = 0.6$, $D = 0.6$, and $(c_{1,2})$ are for $\gamma = 0.2$, $D = 1$, just as in Figure 1.

relaxation of an initial super-critical (sub-crital) gradient x_0 to the critical value x_*. We presented a thorough study of PDFs and information length for different values of the time γ^{-1} and amplitude D of the stochastic forcing as well as for two different initial conditions.

For stationary PDFs, we identified the parameter space for unimodal and bimodal PDFs and compared results with those obtained under the Uniform Coloured Noise Approximation (UCNA) in [22], finding that the UCNA tends to make a stationary PDF of x more bimodal for given parameter values γ^{-1} and D. From time-dependent PDFs, we mapped out attractor structure by computing total information length $\mathcal{L}_\infty = \mathcal{L}(t \to \infty)$ against the location x_0 of a narrow initial PDF of x by using the 'one-observable' version $P(x,t) = \int p(x, f, t)\, df$ and the 'two-observable' version $p(x, f, t)$. In either case, $\mathcal{L}_\infty$ seemed to care about the attractor structure of f in addition to that of x and thus tends to be more unimodal compared with the UCNA results in [22]. This reflects the fact that $\mathcal{L}_\infty$ depends on the history of a PDF evolution which depends on the coupling between x and f. The 'two-observables' version of $\mathcal{L}$ was shown to be significantly greater than the 'one-observable' version, implying the increase in information change with the increase in the number of (observable) variables.

These results underscore the natural, intuitive interpretation of information length as a measure of change in PDFs. Finally, we show how to fine tune an initial joint PDF of x and f for a better agreement with the UCNA results. While the focus of this paper was on the relaxation of a given initial PDF, a fuller description of a self-organised shear flow would require the modelling of a continuous build-up and collapse of shear gradient in time. It remains to address such a dynamical problem in future, e.g. by making γ and/or D time-dependent.

---

[1] Hänggi P and Thomas H 1982 *Phys. Rep.* **88** 207

[2] Risken H 1996 *The Fokker-Planck Equation: Methods of Solution and Applications* (Berlin: Springer)

[3] Klebaner F 2012 *Introduction to Stochastic Calculus with Applications* (London: Imperial College Press)

[4] Gardiner C 2008 *Stochastic Methods, 4th Ed.* (Berlin: Springer)

[5] Jung P 1993 *Phys. Rep.* **234** 175

[6] Lee U, Skinner J, Reinitz J, Rosner M R and Kim E 2015 *PLoS ONE* **10** e0132397

[7] Kim E and Dubrulle B 2001 *Phys. Plasmas* **8** 813

[8] Hänggi P, Marchesoni F and Grigolini P Z 1984 *Physica B* **56** 333

[9] Kim E, Liu H and Anderson J 2009 *Phys. Plasmas* **16** 052304

[10] Newton A P and Kim E 2013 *Phys. Plasmas* **20** 092306

[11] Kim E, Lee U, Heseltine J and Hollerbach R 2016 *Phys. Rev. E* **93** 062127

[12] Nicholson S B and Kim E 2015 *Phys. Lett. A* **379** 83

[13] Nicholson S B and Kim E 2016 *Entropy* **18** 258

[14] Heseltine J and Kim E 2016 *J. Phys. A* **49** 175002

[15] Kim E and Hollerbach R 2017 *Phys. Rev. E* **95** 022137

[16] Hollerbach R and Kim E 2017 *Entropy* **19** 268

[17] Kim E, Tenkès L-M, Hollerbach R and Radulescu O 2017 *Entropy* **19** 511

[18] Tenkès L-M, Hollerbach R and Kim E 2017 *J. Stat. Mech.* 123201

[19] Kim E and Lewis P 2018 *J. Stat. Mech.* 043106

[20] Kim E 2018 *Entropy* **20** 574

[21] Hollerbach R, Dimanche D and Kim E 2018 *Entropy* **20** 550

[22] Jacquet Q, Kim E and Hollerbach R 2018 *Entropy* **20** 613

[23] Jung P and Hänggi P 1987 *Phys. Rev. A* **35** 4464

[24] Wong E and Zakai M 1960 *Ann. Math. Stat.* **36** 1560